(c)2000 American Institute of Aeronautics & Astronautics or Published with Permission of Author(s) and/or Author(s)' Sponsoring Organization.

A00-31117

AIAA 2000-1946

Numerical Analysis of Aircraft High Angle of Attack Unsteady Flows

David B. Findlay
Naval Air Systems Team
Patuxent River, MD

Guru P. Guruswamy
NASA Ames Research Center
Moffet Field, CA

6th AIAA/CEAS
Aeroacoustics Conference
12-14 June 2000 / Lahaina, Hawaii

For permission to copy or republish, contact the American Institute of Aeronautics and Astronautics
1801 Alexander Bell Drive, Suite 500, Reston, VA 20191

Downloaded by NASA AMES Access Login on July 30, 2020 | http://arc.aiaa.org | DOI: 10.2514/6.2000-1946

(c)2000 American Institute of Aeronautics & Astronautics or Published with Permission of Author(s) and/or Author(s)' Sponsoring Organization.

Downloaded by NASA AMES Access Login on July 30, 2020 | http://arc.aiaa.org | DOI: 10.2514/6.2000-1946

Numerical Analysis of Aircraft High Angle of Attack Unsteady Flows

David B. Findlay*
Naval Air Systems Team
Patuxent River, MD
Guru Guruswamy#
NASA Ames Research Center
Moffet Field, CA

Abstract

As breakdown of leading edge separation vortices pass upstream of the empennage surfaces of an aircraft the unsteady wake flow aft of the breakdown engulfs the surfaces. Empennage buffet loads will then result, often causing severe structural fatigue damage. This paper presents a series of results for a twin vertical tail high performacen aircraft configuration at high angles of attack. Computational fluid dynamics analysis involving an overlapping field grid methodology is employed. Solutions were computed on the DoD high performance parallel computer resources. Inter-processor communication was performed with the MPI message passing interface standard library of routines.

A series of angles of attack were considered. Initial steady state solutions show reasonable agreement with experimentally observed surface pressure values and flow field characteristics. Subsequent time-accurate calculations predicted dominant frequency values of the fluctuating surface pressures in close agreement with wind tunnel measurements.

Nomenclature

a_o ..... freestream speed of sound
b ..... wing span
c ..... wing chord
C_p ..... pressure coefficient ($P-P_o/q_o$)
f ..... frequency (Hz)
M ..... Mach number (V/a)
n ..... nondimensional frequency (fb/V)
q ..... dynamic pressure
Re ..... Reynolds number
t ..... time scale
V_o ..... freestream velocity
X ..... chordwise coordinate
Y ..... spanwise coordinate
x,y,z ..... Cartesian Coordinates

α ..... angle of attack
τ ..... nondimensional time (ta_o/d)
ξ,η,ζ ..... curvilinear coordinates

subscripts:
o ..... freestream
p ..... local static pressure

Introduction

High performance aircraft high angle of attack flow characteristics pose technical challenges to an analyst in the areas of geometric complexity, vortex/tail interactions and buffet, vortex breakdown, sharp-edged and boundary-layer flow separations, unsteady flows, and fluid-structure-controls interactions. The existing experimental and computational database provides an opportunity to assess a computational fluid dynamics (CFD) based method when investigating some of these flow features. Figure 1 presents a planform view of an F/

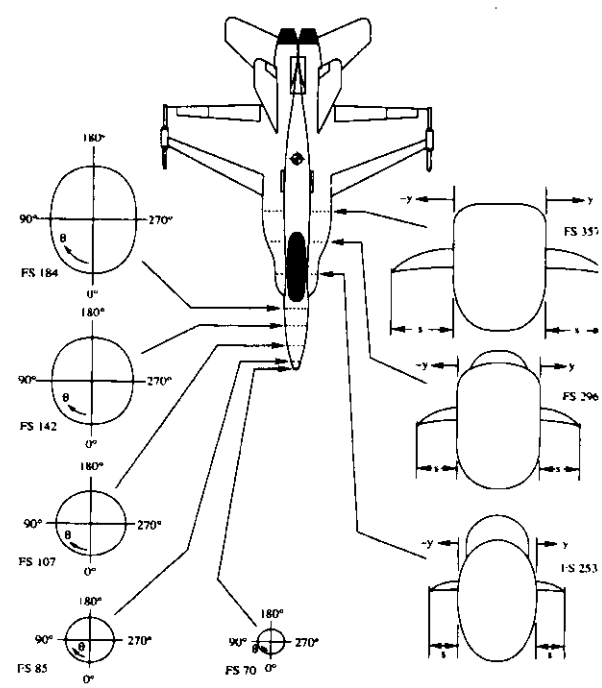

Figure 1: Planform of Aircraft with Pressure Measurement Locations.

A-18A configuration indicating the forebody and LEX stations where surface pressures were

* Head, Advanced Aerodynamics Branch, Member AIAA.
# Senior Research Scientist, AIAA Member.

This paper is declared a work of the U.S. Government and is not subject to copyright protection in the United States.

(c)2000 American Institute of Aeronautics & Astronautics or Published with Permission of Author(s) and/or Author(s)' Sponsoring Organization.

Downloaded by NASA AMES Access Login on July 30, 2020 | http://arc.aiaa.org | DOI: 10.2514/6.2000-1946

measured during wind tunnel and flight tests. The present study includes a CFD investigation of the unsteady aerodynamic vortex/tail interaction and buffet due to high angle of attack flight conditions.

The discussion of the present analysis of the full aircraft configuration tail buffet begins with a description of the F/A-18 grid model. The discussion continues with an analysis of steady-state solutions for a range of angles of attack. Comparisons with available test data for the primary flow features are presented. The next subsection presents a detailed assessment of the unsteady flow features at 30 degrees angle of attack. Comparisons are made with available data.

Due to the three-dimensional, nonlinear, viscous nature of the air flow over the F/A-18 at high angle of attack, the three-dimensional Navier-Stokes equations must be solved to accurately resolve the relevant flow features. The ENSAERO CFD code is employed.[1-7] For the time-accurate computations reported in this study, first-order time accuracy was employed. Since the flow fields of interest involve high Re and include boundary layer flows that are turbulent in nature, the Baldwin-Lomax algebraic turbulence model is used. A modification introduced by Degani and Schiff[8] is used to ensure that the length scales used in vortical flow regions are based on the developing boundary-layer flow on the solid surface and not on those of the separated vortical regions. The F/A-18A geometry is modeled utilizing structured body-fitted overlapping grids. Details of the grid model are discussed in a susequent section. CFD analyses involving an overlapping multi-zone field grid methodology are employed. An enhanced version of the ENSAERO CFD code was developed and employed for this study. Solutions were computed with high performance parallel computers. Inter-processor communication was performed with the MPI message passing interface standard library of routines. The basic fluid dynamics analysis scheme is finite differenced based and allows for first order time-accurate solutions of the Reynolds Averaged Navier-Stokes equations.

Numerical Method of Analysis

The strong conservation law form of the Navier-Stokes equations is used. The thin-layer version of the equations in generalized coordinates are written as

$$\frac{\partial}{\partial\tau}\hat{Q}+\frac{\partial}{\partial\xi}\hat{E}+\frac{\partial}{\partial\eta}\hat{F}+\frac{\partial}{\partial\zeta}\hat{G} = (Re)^{-1}\frac{\partial}{\partial\zeta}(\hat{S}) \qquad (1)$$

where $\hat{Q}$, $\hat{E}$, and $\hat{F}$ are inviscid flux vectors and $\hat{S}$ is the viscous flux vector, all in generalized coordinates. The following transformations were employed in formulating Eq. (1).

$$\begin{aligned} \tau &= t \\ \xi &= \xi(x,y,z,t) \\ \eta &= \eta(x,y,z,t) \\ \zeta &= \zeta(x,y,z,t) \end{aligned} \qquad (2)$$

To solve Eq. (1) an enhanced version of the ENSAERO CFD code is utilized. The present version of the code contains both central and upwind difference flow solvers. For this study, the diagonal form of the centrally based finite-differenced implicit approximate factorization algorithm was employed.[7] Steady state and time-accurate conditions were considered. Due to the extremely small time increments employed in the solution process imposed by stability requirements, the first order time accuracy is considered sufficient. Local Jacobian scaled time stepping is included to accelerate convergence rates in the case of a steady state solution.

A number of enhancements to the code were completed for application in this study. These include: (1) implementation of the code on the IBM SP-2 high performance parallel processing computer, (2) a generalized fluid overlapped zonal boundary interfacing and (3) generalized implementation of a Baldwin-Lomax[7] turbulent eddy viscosity model with the option to include a Degani-Schiff[8] vortex flow modification. This model is used primarily because it is computationally efficient. All viscous computations presented in this paper assume fully turbulent flow. This assumption is considered valid with the high Reynolds numbers considered.

ENSAERO uses finite difference numerics to solve either the discretized Euler or NS equations in multiple field grid zones. Due to the application of the multi-zone approach each zone is solved separately, applying either prescribed flow boundary conditions or interconnecting interpolated conditions along the edges of the zones. This approach is well suited for use with the parallel processing architecture.

Each zone is loaded into the memory of a separate processor. Eq. (1) with appropriate boundary conditions and is solved on each processor (node) at each time level. Interfacing boundary data are interpolated and the updated solution values are passed between connected zones or nodes. With the computation time directly proportional to the number of grid points, this approach is most efficient when all zones contain approximately equal number of grid points.

(c)2000 American Institute of Aeronautics & Astronautics or Published with Permission of Author(s) and/or Author(s)' Sponsoring Organization.

Downloaded by NASA AMES Access Login on July 30, 2020 | http://arc.aiaa.org | DOI: 10.2514/6.2000-1946

Model Definition and Field Grids

Numerical simulation procedures require a discretization of the computational domain. For a simple configuration, the discretization procedure may only consist of creation of a single grid engulfing the entire region of concern. However, for realistic complex three-dimensional geometries, such as the F/A-18A aircraft, a multiple zonal gridding approach is required. For the case of structured field grids, both patched and overlapping zonal schemes have been used successfully to simulate the viscous three-dimensional flow around complex geometries. The overlapping zonal scheme is considerably more flexible. The task of grid generation is made easier because the scheme does not require neighboring grids to match along common grid lines. This section discusses the discretization procedure, which consists of geometry definition, surface and volume grid generation, zoning strategy and the establishment of proper inter-zonal communications.

Shown in Figure 2 is an illustration of the surface

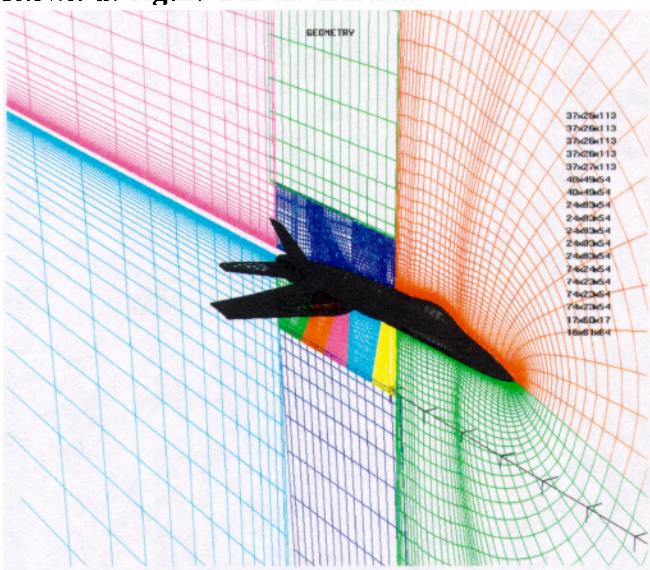

Figure 2: F/A-18A CFD Multi-Zone Grid Model.

and symmetry plane computational grids for the complete F/A-18A aircraft grid model. A total of 18 zones combine to represent the fuselage, LEX, wing and empennage surfaces. To allow for reduced modeling and computing requirements, a simplified model was used. In particular, small protuberances (e.g., antenna fairings) and small components (such as missile launchers, etc.) are neglected due to an expected insignificant effect on the main features of the flowfield. In addition, the wing LE flap/LEX gap were fared over. The inlet face was modeled as a solid surface rather than a grid interface. In past studies, similar approximations have been exploited with little or no noticeable influence on the computed primary flow features[9-13].

The aircraft surface definition was originally given in terms of IGES files. A sting was added to the aft end of the computational model. The leading-edge flap surface grid was obtained by deflecting the wing surface grid around the hinge line, which is located at the 20% chord position. A small spanwise blended region was assumed between the wing root section and the flap. This region was employed to transition between the wing root/LEX intersection and the actual leading-edge flap deflection, alleviating the arduous task of modeling the flap root gap region. Furthermore, the gap between the inboard and outboard flaps, as well as any gaps along the hinge lines were not simulated. Finally, the horizontal tail was set at 7 degrees nose down. This corresponds to the proper scheduled deflection angle for the 30 degrees angle of attack flight condition.

After all the surfaces were defined, surface grids were obtained by spline-fitting the given surface points. Control points were placed at specific locations to preserve corners, junctions of wings and tails, etc. A clustering capability in both directions defining the surface was employed to place grid points where they were needed to best resolve the primary flow features. The field grid system consists of 18 zones.

Discussion of Results

Steady-State Analysis

The half-body grid system modeling the F/A-18 geometry was employed to compute high angle of attack at a typical condition of $M = 0.2$, $\alpha = 30$ degrees and $Re = 11$ million. While most of the analysis was made at this condition, additional calculations included $\alpha = 20$ degrees for the same Mach and Reynold numbers. Using variable time stepping throughout the CFD grid, an initial pseudo-steady-state solution was computed. Contours of the local total pressures normalized by the freestream total pressure at various cross-flow planes, along with streamlines representing LEX separation vortex cores, are shown in Figure 3. Total pressure contours are often used to indicate regions of dissipation losses within the separated flow regions. The normalized total pressure contours of Figure 3 illustrate the presence of a well-organized LEX vortex flow up to about the LEX/wing leading edge juncture. The LEX vortex core region, highlighted by the lower values of total pressure

(c)2000 American Institute of Aeronautics & Astronautics or Published with Permission of Author(s) and/or Author(s)' Sponsoring Organization.

Downloaded by NASA AMES Access Login on July 30, 2020 | http://arc.aiaa.org | DOI: 10.2514/6.2000-1946

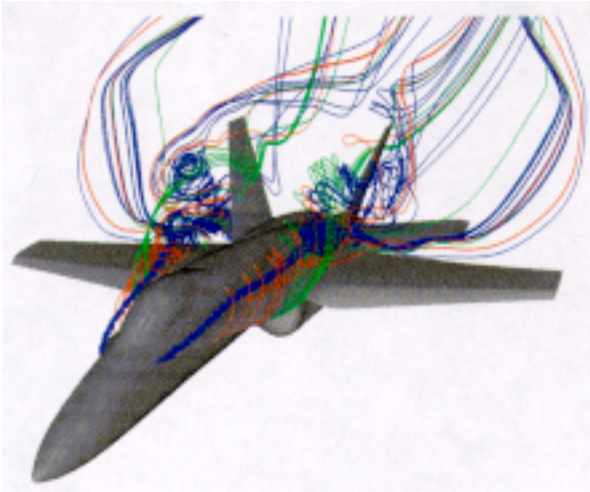

Figure 3(a): Flow Visualization Particale Traces of Computed LEX Vortex at 30 degress Angle of Attack.

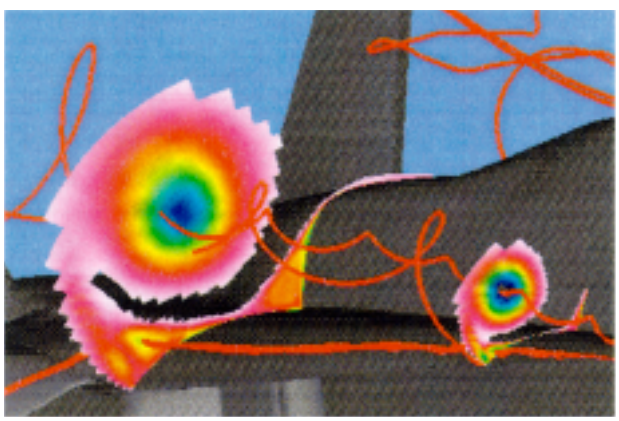

Figure 3(b): Flow Visualization Total Pressure Contours of Computed LEX Vortex at 30 degress Angle of Attack.

(indicated by the grey shades of contours), experienced breakdown evident by the expansion of the ordered core particle traces.

In general, the air flow is essentially steady upstream of the vortex breakdown location. However, the vortex breakdown location and the downstream spiraling wake are considered highly unsteady. The initial steady-state solutions at 30 degrees angle of attack, obtained with the half span medium (1.5 millions points) and fine (3.5 million points) density grid models, were considered in comparisons with experimental data of surface pressures at distinct sections on the forebody and LEX upstream of the breakdown location. The comparison on the forebody is depicted in Figures 4.

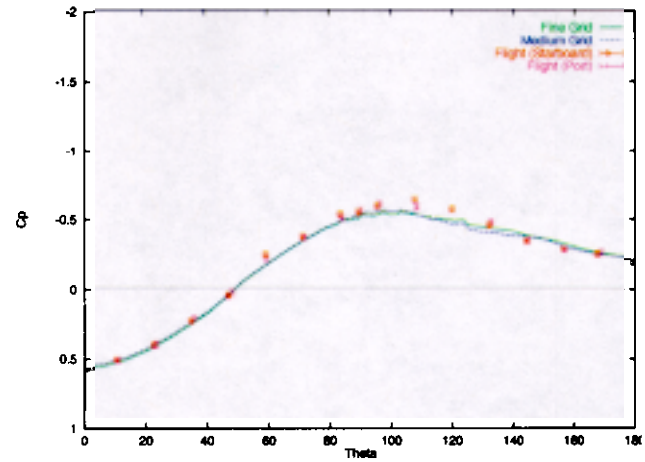

Figure 4(a): Nose Surface Pressure Coefficient Values at Fuselage Station 85. inches.

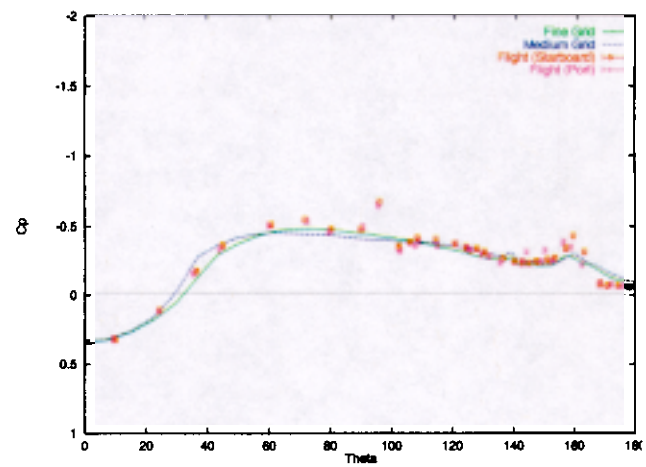

Figure 4(b): Nose Surface Pressure Coefficient Values Fuselage Station 142. inches.

The comparisons indicate a fairly good agreement between the computational results and flight test data. The surface pressure coefficient values computed for the forebody indicated the presence of a vortex separating from the nose region at approximately 90 degrees from the bottom center line. For the forebody comparison, both the fine and medium grid results compared equally well with the test data. The slight discrepancy may be attributed to the fact that in flight there is a small region of laminar/transitional shear flow near the nose, while in the computations the flow is assumed to be fully turbulent. The discrepancy at 95 degrees at fuselage station 142 is due to a small antenna fairing which is neglected in the computations. It is obvious that the effect was local and does not affect the flow elsewhere.

.(c)2000 American Institute of Aeronautics & Astronautics or Published with Permission of Author(s) and/or Author(s)' Sponsoring Organization.

Downloaded by NASA AMES Access Login on July 30, 2020 | http://arc.aiaa.org | DOI: 10.2514/6.2000-1946

Comparisons of computed LEX surface pressure coefficient values with in-flight measured values are shown in Figure 5. Similar to the earlier surface

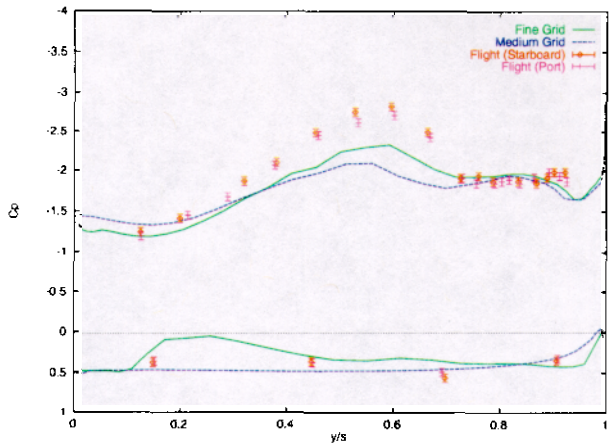

Figure 5(a): LEX Surface Pressure Coefficient Values at Fuselage Station 253. inches.

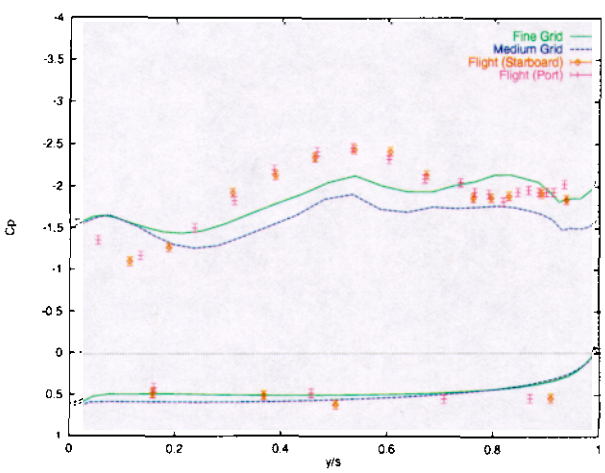

Figure 5(b): LEX Surface Pressure Coefficient Values at Fuselage Station 296. inches.

pressure comparisons of the delta wing calculations, the LEX upper surface results indicated suction peaks attributed to the presence of the main leading edge separation vortex. The results shown for the medium grid density compare well (within a few percent) with computed results presented by Rizk, et.al.[12]. A noticeable improvement is seen in the results of the fine grid case over the medium grid for the LEX surface pressures. However, the medium grid results capture the primary influence of the vortex flow. The computed magnitudes were lower than the measured values due to the grid density. Again, the intent of the present study is to explore the feasibility of the methods and maintain a manageable computational requirement. The requirement for computing time accurate tail loads with the fine grid is beyond the limits of available computational resources. Therefore, a moderate size of grid dimensions was selected, so that the main features of the flowfield are maintained for evaluation while computational resources were managed. As such, the medium density grid CFD model was employed.

Figure 6 shows Flow visualization of in flight vortex

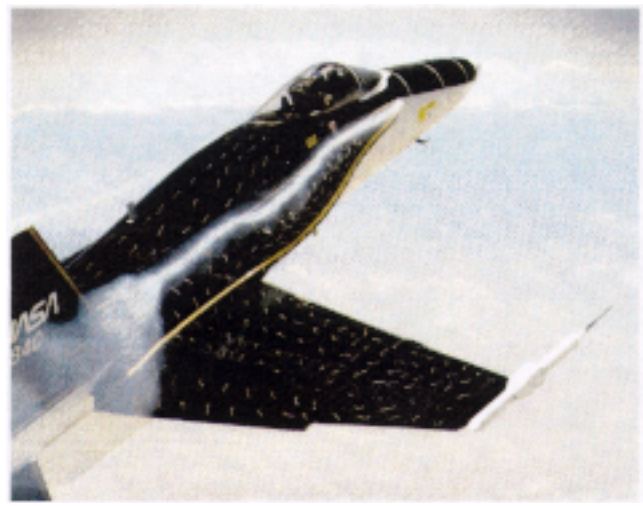

Figure 6(a): The F/A-18 Aircraft Experiencing Tail Buffet Loads Near $\alpha \sim 20$ degrees (courtesy of NASA Dryden).

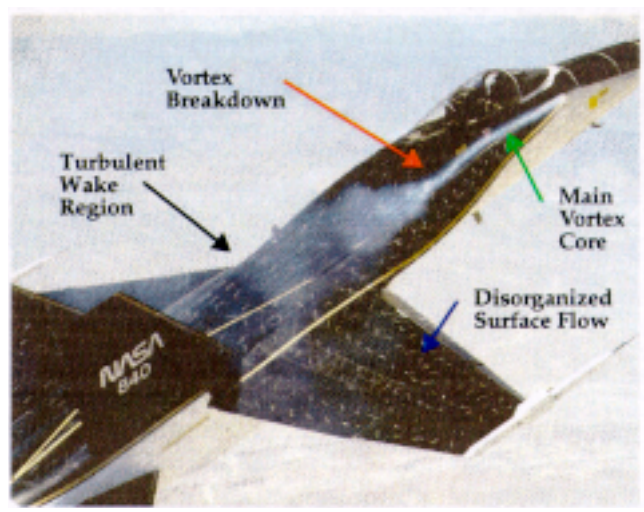

Figure 6(b): The F/A-18 Aircraft Experiencing Tail Buffet Loads Near $\alpha \sim 30$ degrees (courtesy of NASA Dryden).

flows at high angle of attack. Figure 7 depicts the computed differences within the primary vortex flow region for angles of attack of 20 degrees and 30

(c)2000 American Institute of Aeronautics & Astronautics or Published with Permission of Author(s) and/or Author(s)' Sponsoring Organization.

Downloaded by NASA AMES Access Login on July 30, 2020 | http://arc.aiaa.org | DOI: 10.2514/6.2000-1946

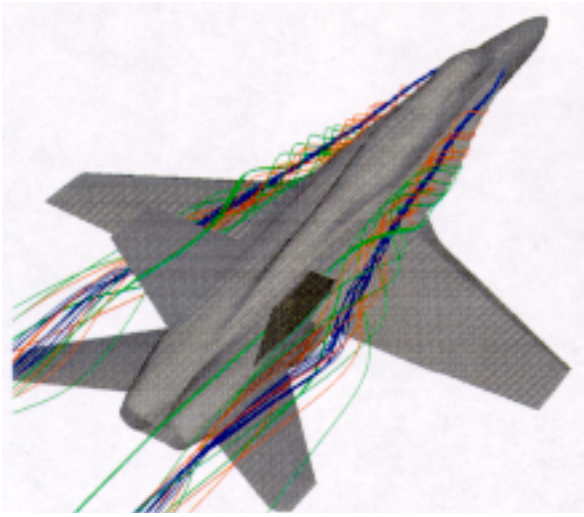

Figure 7(a): Perspective View of LEX Vortex Portrayed with Partial Traces at 20 degrees Angle of Attack.

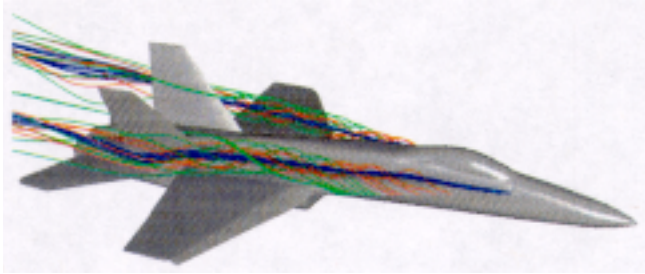

Figure 7(c): Side View of LEX Vortex Portrayed with Partial Traces at 20 degrees Angle of Attack.

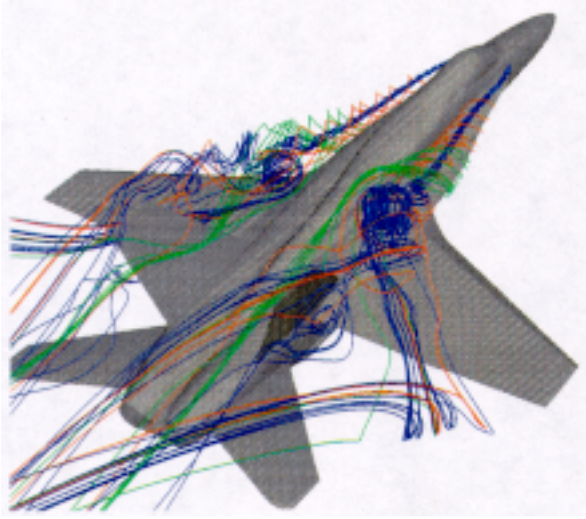

Figure 7(b): Perspective View of LEX Vortex Portrayed with Partial Traces at 30 degrees Angle of Attack.

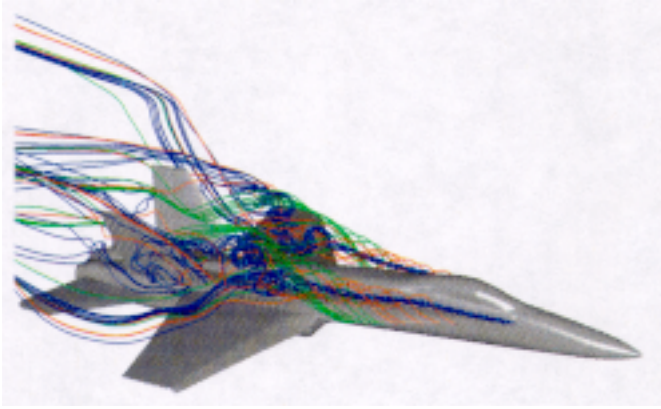

Figure 7(d): Side View of LEX Vortex Portrayed with Partial Traces at 30 degrees Angle of Attack.

degrees. For the case of 20 degrees, the particle traces show a primary vortex flow structure which emanated from the LEX leading edge and passed over the leeward side of the aircraft. The vortex eventually passed by the vertical tail. The bulk of the vortex was seen to pass on the outboard side of the tail. The vortex core was then seen to open slightly near the tail, indicating the onset of vortex breakdown. This is consistent with the flow visualization of in flight vortex flows shown in Figure 6. The particle traces at a given time showed the change in vortex breakdown location leading to the pronounced unsteady wake impinging on the tail at 30 degrees angle of attack. Although the flow was expected to be unsteady, the traces through the steady-state computations provided a useful qualitative perspective of the primary flow features.

Unsteady Flow Analysis

Since the main objective of the current work was to study the tail buffet, unsteady analysis including time histories of tail pressure loading was considered essential. As mentioned before, the flow is expected to be primarily steady upstream of the vortex breakdown location. However, the breakdown location and spiral flow region aft of the

(c)2000 American Institute of Aeronautics & Astronautics or Published with Permission of Author(s) and/or Author(s)' Sponsoring Organization.

Downloaded by NASA AMES Access Login on July 30, 2020 | http://arc.aiaa.org | DOI: 10.2514/6.2000-1946

breakdown are unsteady. This is manifested as an unsteady pressure field engulfing the tail surface. The unsteady pressure field impeding on a rigid tail surface is the focus of this section.

Pressure coefficient values were computed and time histories were saved for specific points on the vertical tail surface. Figure 8 illustrates the locations

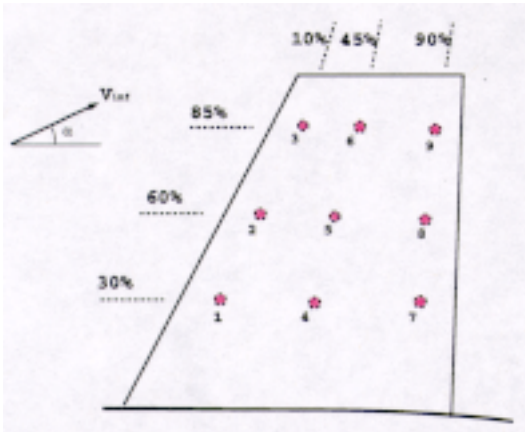

Figure 8: Sketch of F/A-18 Vertical Tail with Locations of Surface Pressure Coefficient Calculated Values Considered.

of these points. These locations were selected to match up with the location of measurements taken on the inboard and outboard side of the tail. Values computed near the center of the tail surface for the inboard and outboard sides of the tail, as well as the difference (inboard-outboard) between these two values, are shown in Figure 9. Values are given as a

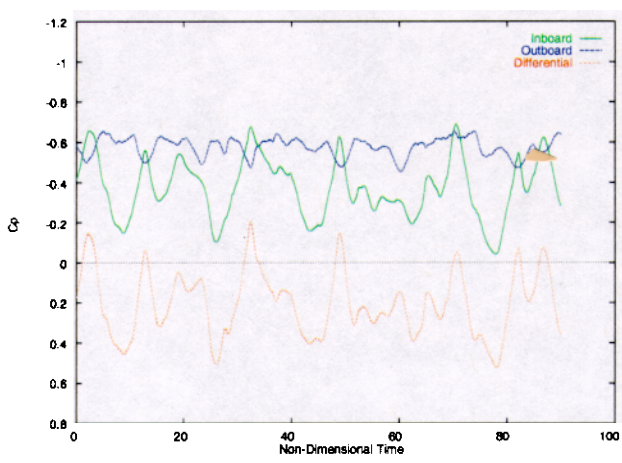

Figure 9: Time History of Surface Pressure Coefficient on Rigid Vertical Tail at Location 5 (45% Chord and 60% Span), for 30 degrees Angle of Attack.

function of time non-dimensionalized by freestream speed of sound and wing root chord. While the mean of the inboard surface C_p values indicated less suction than did the C_p on the outboard surface, the inboard computed maximum peak values exceeded those of the outboard surface. This is due to the fact that the majority of the vortex breakdown turbulent wake region of flow passed downstream inboard of the tail. For the most part, the computed time accurate C_p values shown in Figure 9 imply that appreciable portions of the inboard and outboard surface pressures were 180 degrees out of phase.

The time history at a series of chordwise locations near mid-span of the vertical tail on the inboard surface are shown in Figures 10 and 11. The maximum magnitudes consistently occurred at location 2 (nearest to the leading edge) and the minimum peak suctions consistently occurred at location 8 (nearest to the trailing edge). The computed time dependent C_p experienced inboard surface suction peaks closely followed by outboard surface suction valleys. Conversely, the inboard suction valleys were often closely followed by outboard suction peaks. This result at location 5, near mid-chord, closely resembled the C_p at location 2 with the exception of a temporal phase shift and a reduction in mean suction value. These results are expected due to the effect of the diminishing vortex strength via dissipation and the influence of the tail. While the time variation of C_p at location 8 followed a similar trend to those of locations 2 and 5, the average turbulence intensity was reduced, and the higher frequency components became more noticeable. Another interesting observation from Figure 10(a) is that, although the peak and mean suction C_p steadily reduced as one travels toward the trailing edge, the local valleys reached minimum values as a function of relative chord location. This can be attributed to the tendency of the flow to recirculate outboard of the tail.

The time history at a series of spanwise locations near mid-chord of the vertical tail on the inboard surface are shown in Figure 11. Similar to the chordwise comparison of Figure 10, the time histories of C_p maintained consistent trends spanwise along a constant percent chord. That is, a nearly consistent phase relation occurred initially nearest to the root and eventually traveled to the tip. However, unlike the chordwise comparison, the maximum peak and valley suction values were almost exclusively associated with the location nearest to the root, and the minimum peak and valley values were associated with the location nearest to the tip. Similar to the chordwise comparison, the variation in maximum suction peak was more noticeable than the variation in local

.(c)2000 American Institute of Aeronautics & Astronautics or Published with Permission of Author(s) and/or Author(s)' Sponsoring Organization.

Downloaded by NASA AMES Access Login on July 30, 2020 | http://arc.aiaa.org | DOI: 10.2514/6.2000-1946

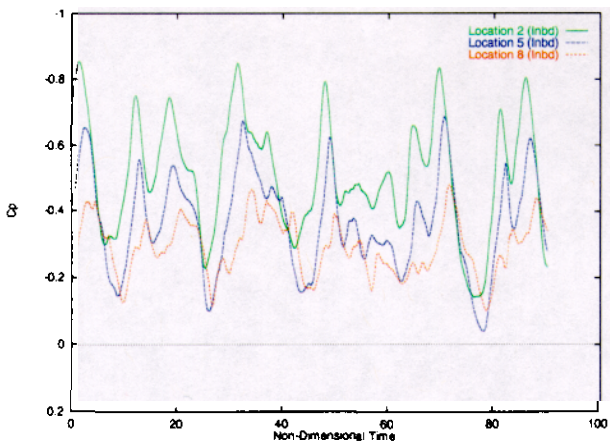

Figure 10: Time History of Computed Inboard Surface Pressure Coefficient on Rigid Vertical Tail at Various Chordwise Locations.

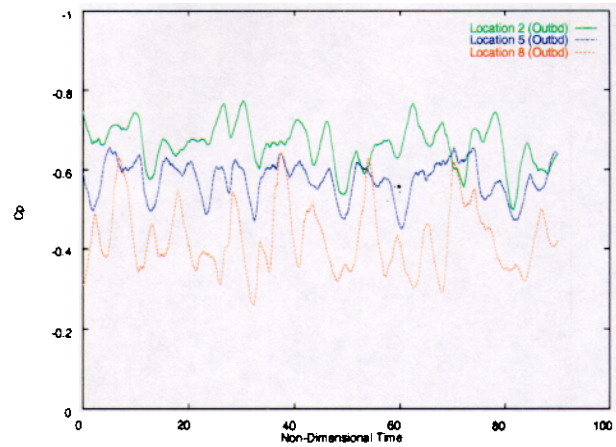

Figure 12: Time History of Computed Outboard Surface Pressure Coefficient on Rigid Vertical Tail at Various Chordwise Locations.

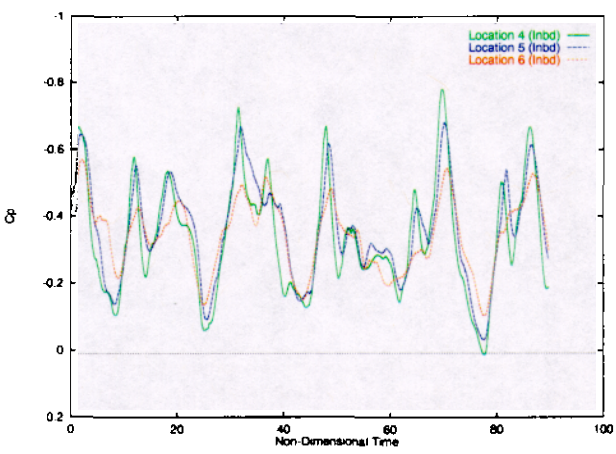

Figure 11: Time History of Compute Inboard Surface Pressure Coefficient on Rigid Vertical Tail at Various Spanwise Locations.

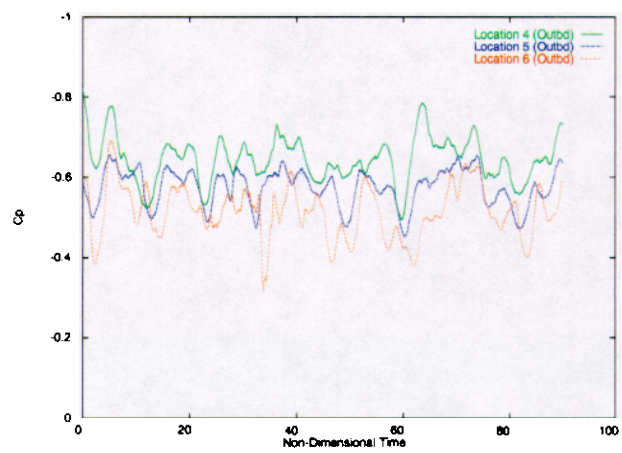

Figure 13: Time History of Computed Outboard Surface Pressure Coefficient on Rigid Vertical Tail at Various Spanwise Locations.

valleys.

Figures 12 and 13 illustrates the time dependent C_p value on the outboard surface of the vertical tail at 30 degrees angle of attack. Compared to Figures 10 and 11, fluctuations were lower than seen on the inboard surface. Similar to the results on the inboard side, location 5 closely resembled location 2 with a slight time lag and shift toward higher mean suction values. The highest suction was nearest to the leading edge with less suction present as one traverses chordwise aft. These same trends are seen in the results computed on the inboard side. Unlike the inboard surface results, the phase seemed to fluctuate (plus and minus) between location 2 and location 5 implying reversed flow for periods of time. This is supported by the particle traces discussed for Figure 7. A noticeable correlation appeared between the leading edge flow and the midchord flow. Less correlation appeared to exist chordwise as one approaches the trailing edge. Value at locations 2 and 5 in Figure 7 represent nearly periodic losses in suction, while location 8 indicate an increase in suction.

Referring to Figure 13 for the spanwise comparison of outboard surface pressures, distinct differences are shown from the C_p time histories computed on the inboard surface. Some of the differences are: 1.)

(c)2000 American Institute of Aeronautics & Astronautics or Published with Permission of Author(s) and/or Author(s)' Sponsoring Organization.

Downloaded by NASA AMES Access Login on July 30, 2020 | http://arc.aiaa.org | DOI: 10.2514/6.2000-1946

clearer shift in mean values as one proceeds spanwise outboard, 2.) more prominent higher frequency turbulence on the outboard surface, and 3.) more distinctive time histories from location to location spanwise on the outboard surface than on the inboard surface.

Figure 14 shows comparisons of the time histories of

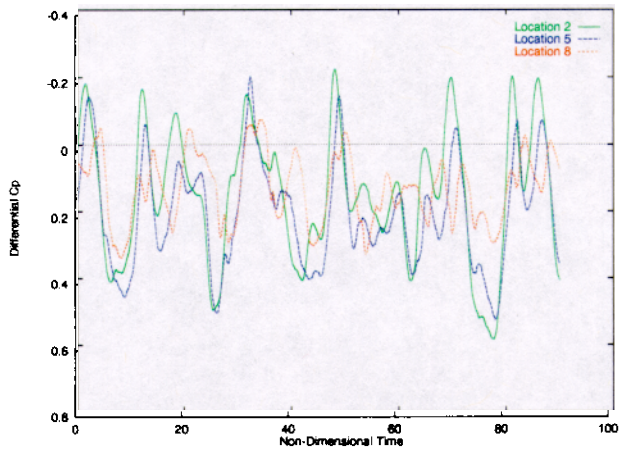

Figure 14(a): Time History of Differential Surface Pressure Coefficient on the Rigid Vertical Tail at Various Chordwise Locations.

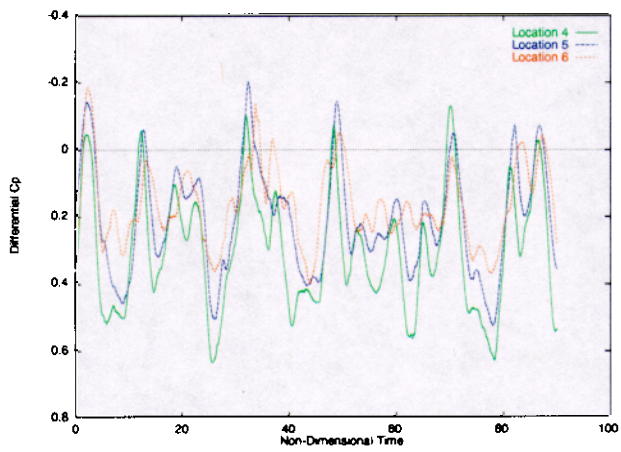

Figure 14(b): Time History of Differential Surface Pressure Coefficient on the Rigid Vertical Tail at Various Spanwise Locations.

computed differential surface pressure coefficient at various locations on the vertical tail. As with the inboard C_p values, the differential C_p values followed a general overriding trend consistent across the complete tail surface. Also, similar to the inboard surface, the differential C_p nearest to the trailing edge and tip location lagged those nearest to the leading edge and root, respectively.

The mean value of an ensemble of a signal such as the C_p time history at a specific location provides insight as to the relative strength of the signals. The standard deviation of the signal gives a broad weighting and serves as a composite magnitude of the unsteadiness of the pressures. These functions can be used to describe the relative character of the time dependent buffet pressures at separate locations on the tail. The locations for which results will be presented are depicted in Figure 8. Figure 15(a) displays the distribution of mean and standard

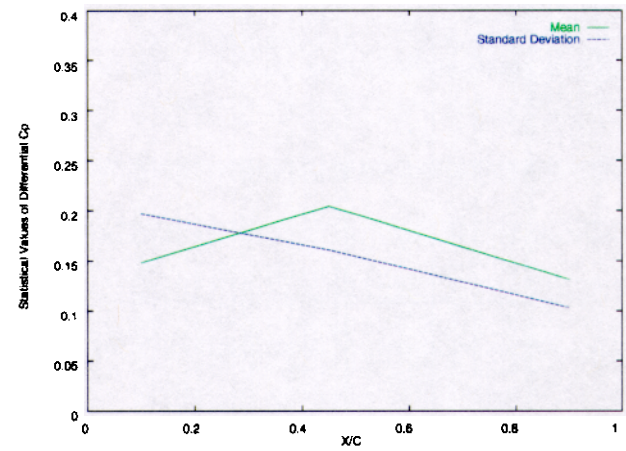

Figure 15(a): Mean and Standard Deviation of Differential Pressure Coefficient on the Rigid Vertical Tail at Various Chordwise Locations for a 60% Span Section.

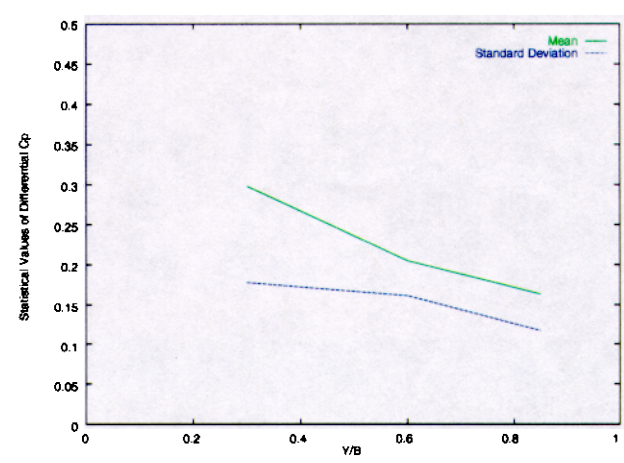

Figure 16(b): Mean and Standard Deviation of Differential Pressure Coefficient on the Rigid Vertical Tail at Various Spanwise Locations for a 45% Chord Section.

(c)2000 American Institute of Aeronautics & Astronautics or Published with Permission of Author(s) and/or Author(s)' Sponsoring Organization.

Downloaded by NASA AMES Access Login on July 30, 2020 | http://arc.aiaa.org | DOI: 10.2514/6.2000-1946

deviation of differential surface pressure along a chordwise section near the midspan. Similarly, Figure 15(b) displays the distributions of mean and standard deviation of differential pressure values along a midchord spanwise section. With respect to the standard deviation, s, distributions of Figures 15 and 16, depict a clear trend of the highest s values nearest to the leading edge and root. The s values monotonically decreased toward the trailing edge and tip of the tail. This is consistent with the argument that the locations closest to the vortex breakdown location are expected to experience the highest buffet pressures. This trend can also be attributed to the reduced impact of the vortex flow as it is dissipated while traveling downstream. Although not shown, the standard deviation values of the unsteady pressures were greater on the inboard surface at this angle of attack than on the outboard side. This is due, in part, to the fact that the center of the vortex breakdown flow region passed inboard of the tail. Furthermore, for the chordwise row of locations, the leading edge locations had the highest standard deviation values while the trailing edge stations had the lowest values.

In terms of the distributions of mean differential C_p, the trend was consistent with that of s in the spanwise direction, that is, the highest values occurred nearest to the root. However, the maximum mean buffet C_p value resided near the midchord. This same trend was seen in the experimental results of Moses[16] for a sub-scale F/A-18 wind tunnel model. The implication is that a loss of suction on the outboard side of the tail relative to the inboard side is caused by the presence of the tail surface shielding the outboard side from the vortex flow.

The power spectral density (PSD) curves provide a means for comparing the magnitudes with respect to frequency and identify the spectral content of the unsteady pressures. Employing the MATLAB[14] signal processing software package, a PSD analysis was performed on the C_p time histories. The length of the total time period for which solutions were computed was approximately one second. The time histories were assumed to be stationary and were divided into three equal segments. While all three segments indicate similar spectral traits, certain distinctions are displayed. The peak of the first segment occurred at n = 0.4, which is the same as the average. However, the third segment contained peak spectral values 50 percent higher. The results demonstrate that the selection of a time period that is sufficiently long is important to allow for adequate accuracy. The CFD result of Reference [9] gave a value that significantly over predicted the characteristic frequency compared to the experiments.

A comparison of the dominant frequencies obtained from the PSD analysis of the pressure histories, with measured results of Reference [15] and CFD results of references [9] and [11] is presented in Figure 17.

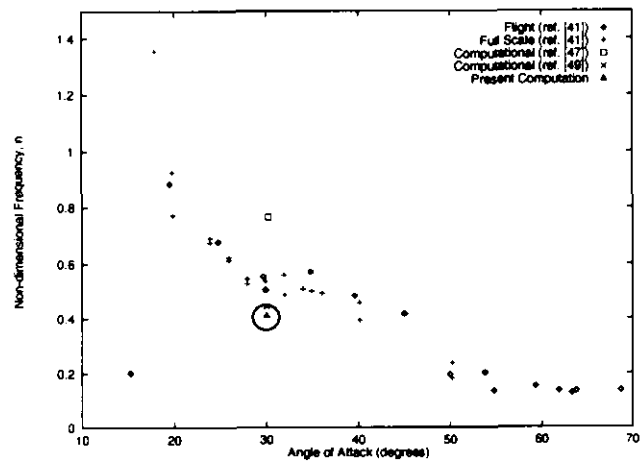

Figure 17: A Comparison of Nondimensional Frequency of Peak PSD of Surface Differential Pressure Coefficient on the Vertical Tail at 60% Span, 45% Chord.

The present results compare fairly well with the experimental results.

The cross-correlation function of computed differential pressure coefficient at distinct points on the tail are shown in Figure 18. The shortest time lag existed between the events at location 2 and location 5. However, the highest correlation value was between location 5 and location 8. The longest time lag was between signals at location 2 and location 8, which also corresponds to the lowest relative correlation value. This indicates that the flow direction became more chordwise in the aft region of the tail.

The lead or lag in times shown in Figure 18 pertaining to the peak correlation values can be thought of as time delays. The time delays indicate the time needed for the pressure wave to move between the two locations. These time delays, along with the associated distances can be used to compute local chordwise convective velocities. The non-dimensional time delays listed in Table I indicate the time required at α = 30 degrees and Mach = 0.243 for the differential pressure wave to move downstream along the tail. Reviewing the results of Table I, an average normalized convective velocity is 0.69. This result agrees well with experimental results by Moses[16]. Using a 16% F/A-18A wind tunnel model, Moses reported a streamwise normalized convective velocity of 0.70 at

(c)2000 American Institute of Aeronautics & Astronautics or Published with Permission of Author(s) and/or Author(s)' Sponsoring Organization.

Downloaded by NASA AMES Access Login on July 30, 2020 | http://arc.aiaa.org | DOI: 10.2514/6.2000-1946

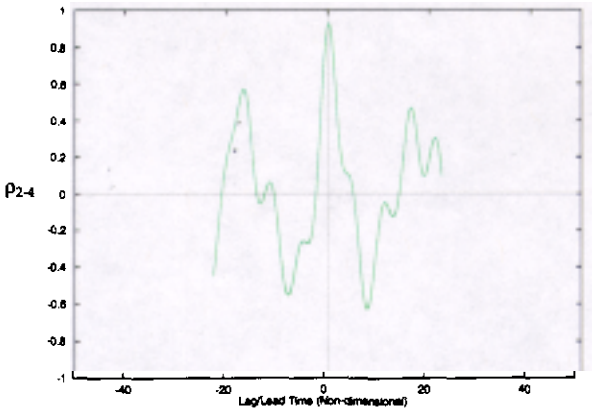

Figure 18(a): Cross-Correlation of Surface Differential Pressure Coefficient on the Rigid Vertical Tail Between Locations 2 and 4.

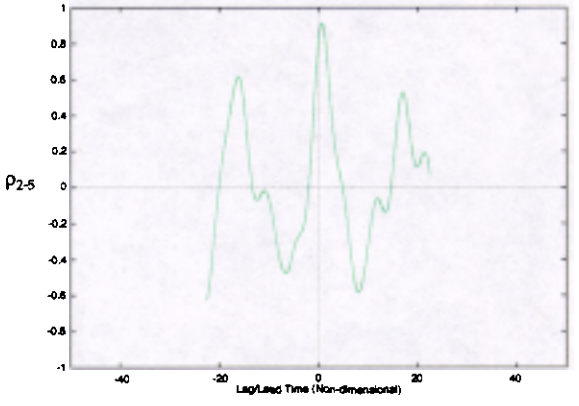

Figure 18(b): Cross-Correlation of Surface Differential Pressure Coefficient on the Rigid Vertical Tail Between Locations 2 and 5.

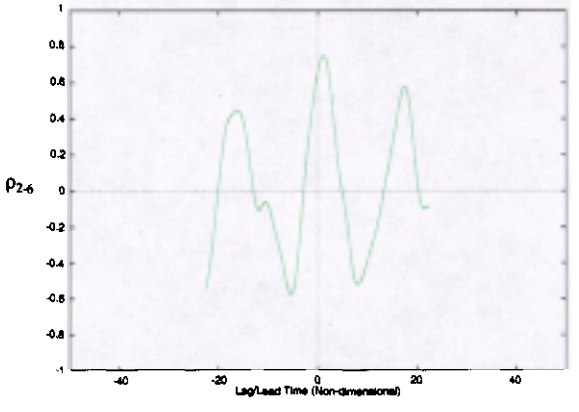

Figure 18(c): Cross-Correlation of Surface Differential Pressure Coefficient on the Rigid Vertical Tail Between Locations 2 and 6.

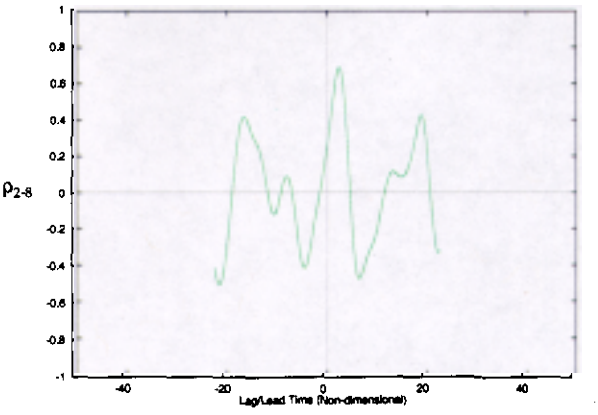

Figure 18(d): Cross-Correlation of Surface Differential Pressure Coefficient on the Rigid Vertical Tail Between Locations 2 and 8.

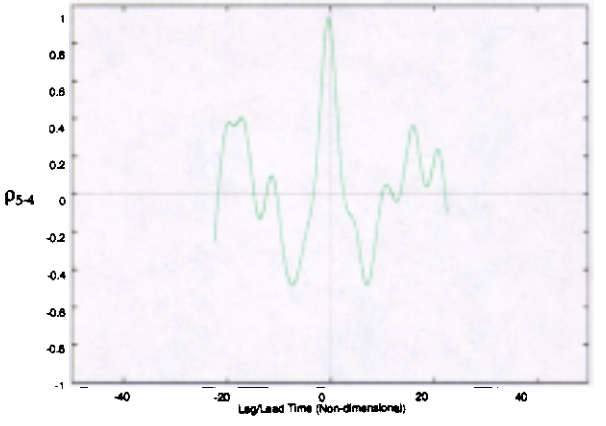

Figure 18(e): Cross-Correlation of Surface Differential Pressure Coefficient on the Rigid Vertical Tail Between Locations 5 and 4.

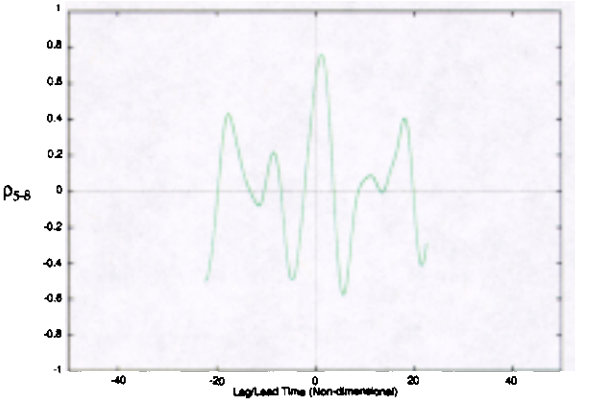

Figure 18(f): Cross-Correlation of Surface Differential Pressure Coefficient on the Rigid Vertical Tail Between Locations 5 and 8.

(c)2000 American Institute of Aeronautics & Astronautics or Published with Permission of Author(s) and/or Author(s)' Sponsoring Organization.

Downloaded by NASA AMES Access Login on July 30, 2020 | http://arc.aiaa.org | DOI: 10.2514/6.2000-1946

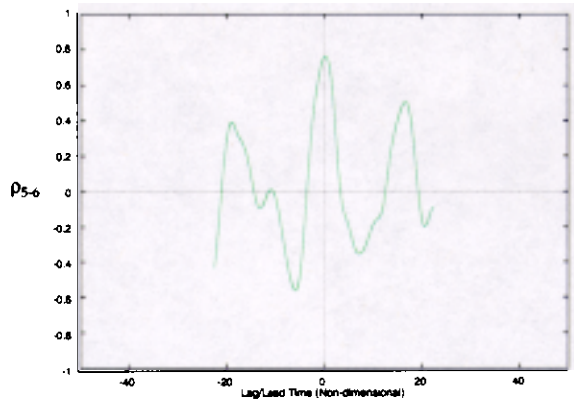

Figure 18(g): Cross-Correlation of Surface Differential Pressure Coefficient on the Rigid Vertical Tail Between Locations 5 and 6.

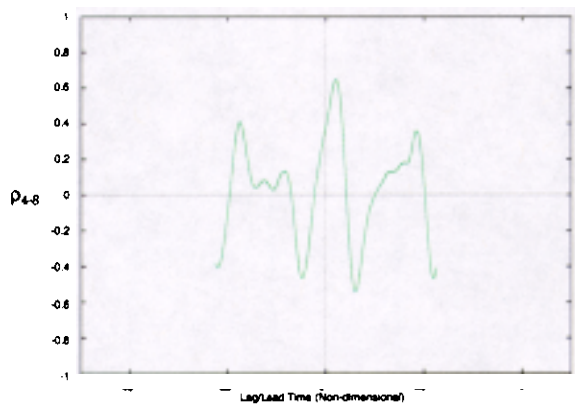

Figure 18(h): Cross-Correlation of Surface Differential Pressure Coefficient on the Rigid Vertical Tail Between Locations 4 and 8.

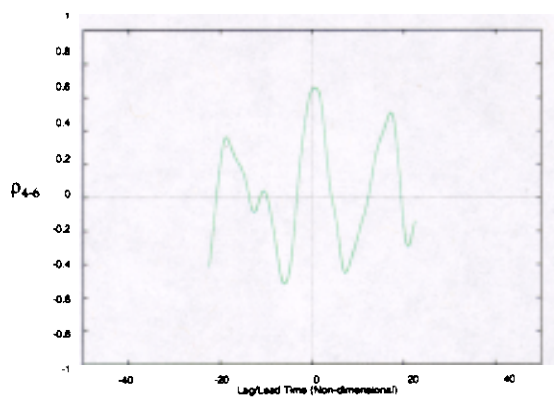

Figure 18(i): Cross-Correlation of Surface Differential Pressure Coefficient on the Rigid Vertical Tail Between Locations 4 and 6.

Table I: Summary of Normalized Chordwise Convective Velocity Computed from Cross-Correlation of Differential Surface Pressures.

Coefficient	ρ_{2-5}	ρ_{2-8}	ρ_{5-8}
Maximum Value	0.913	0.689	0.761
Non-dimensional Time of Occurrence	0.7	2.3	1.2
Non-dimensional Convective Vel.	0.98	0.58	0.53
Average Conv. Velocity	0.69		
Experimental Ave. Conv. Vel. (α = 34 deg.) (from Reference [16])	0.70		

34 degrees angle of attack. This value was evaluated from maximum values of cross-correlation functions of differential surface C_p. Although results were not given for 30 degrees angle of attack, mention was made that the convective velocities varied only slightly across this range of angle of attack. Table I shows a trend of less convective velocity the further aft on the tail that one travels. This trend agrees with the trend of the experimental measurements reported by Moses.

Conclusions and Recommendations

A detailed assessment of the computed unsteady vortex breakdown flow known to cause aircraft tail buffet was achieved. A study of the flow features, present at high angle of attack conditions, for configurations known to experience tail buffet has expanded the understanding of features of these types of flows.

A full configuration F/A-18A aircraft computational fluid dynamics grid model was developed. The model was employed to perform a computational study of steady and unsteady calculations for rigid tails. At each step in the process, computed flow features of significance to buffet were revealed, and discussed, in order to provide a greater understanding of the underlying traits of the flows native to the tail buffet problem.

The following conclusions can be drawn from the present study:

(c)2000 American Institute of Aeronautics & Astronautics or Published with Permission of Author(s) and/or Author(s)' Sponsoring Organization.

Downloaded by NASA AMES Access Login on July 30, 2020 | http://arc.aiaa.org | DOI: 10.2514/6.2000-1946

- Results show reasonable agreement with measured dominant frequencies of the buffet pressures. The trend with angle of attack agrees with measured results. Increases in flowfield grid fidelity showed improvements in surface pressures for steady-state calculations.
- Time histories of computed surface pressures with the F/A-18A model show harmonic fluctuations. Cross-correlations of the pressure across the tail indicate strong single-path correlations with small lag/lead times. The lag/lead times represent a chordwise convective velocity of 70% freestream, which matches measured data.
- Spectral analysis reveals the computed time-dependent surface pressures to have a characteristic frequency very near the first mode of the tail structure.

To extend beyond the present work a few options can be considered. A list of recommendations is given below:

- Higher-order spatial differencing schemes can provide improved spatial accuracy, while only slightly increasing the computational overhead relative to directly increasing grid density. This is especially desirable in the vicinity of the vortex core.
- Utilization of solution adaptive flowfield grids is an approach to accounting for large variations of flow variables in the region of the primary vortex. This approach is expected to improve accuracy up to the vortex breakdown location. Some difficulty might arise in attempting to adapt the grid to the unsteady wake flow region. However, a scheme can be envisioned that would adapt to the initial steady state solution, allowing some automation of the process.
- Continued advances in computer technology and the increased number of systems becoming more readily available for regular use serves to improve the ability to include finer grid fidelity.
- Dynamic aeroelastic analysis for air-vehicle development purposes is becoming a viable option. Therefore, future work could consider employing a time-accurate flow solver in a tightly-coupled dynamic aeroelastic analysis of the full configuration.
- Recent experimental studies, focusing on buffet alleviation, have employed both active and passive flow control methods. In addition, active piezoelectric actuation impended within the structure are being studied. An ability to reduce the structural response of the vertical tail was experimentally demonstrated utilizing each of these forms of control systems. Computational studies have the ability to predict trends of these systems as a function of angle of attack, dynamic pressure, and mass and/or stiffness distributions. The analysis can provide for better development these types of systems.

Finally, future air-vehicles such as the Joint Strike Fighter (JSF), both versions of which have relatively sharp cornered forebody/wing junctions, may be prone to vortex breakdown causing buffeting loads. The hope is that the present work will provide insight, guidance, and motivation toward employing unsteady Navier-Stokes-based dynamic analysis to aid the development of these and other advanced air-vehicles.

References

1. Guruswamy, G.P., "Unsteady Aerodynamics and Aeroelastic Calculations for Wings Using Euler Equations," AIAA Journal, Volume 28, Number 3, March 1990.

2. Guruswamy, G.P., "Vortical Flow Computations on Swept Flexible Wings Using Navier-Stokes Equations," AIAA Journal, December 1990.

3. Guruswamy, G.P., and Byun, C., "Fluid-Structural Interactions Using Navier-Stokes Flow Equations Coupled with Shell Finite Element Structures," AIAA Paper 93-3087, AIAA 24th Fluid Dynamics Conference, Orlando, FL, July 1993.

4. Byun, C. and Guruswamy, G.P., "Wing-Body Aeroelasticity Using Finite-Difference Fluid/Finite-Element Structural Equations on Parallel Computers," AIAA 94-14-1487-CP, 1994.

5. Findlay, D., "Numerical Analysis of Vertical Tail Buffet", AIAA 97-0621, January 1997.

6. Byun, C. and Guruswamy, G.P., "Aeroelastic Computations on Wing-Body-Control Configurations on Parallel Computers," Journal of Aircraft, Volume 35, No. 2, March 1998.

7. Findlay, D., "A Numerical Study of Aircraft Empennage Buffet", Ph.D. Dissertation, Georgia Institue of Technology, Atlanta, GA, June 1999.

8. Degani, D., and Schiff, L.B., "Computation of Turbulent Supersonic Flows Around Pointed Bodies Having Cross Flow Separation," Journal of Computational Physics, Vol. 66, No. 1, September 1986, pp. 173-196.

(c)2000 American Institute of Aeronautics & Astronautics or Published with Permission of Author(s) and/or Author(s)' Sponsoring Organization.

Downloaded by NASA AMES Access Login on July 30, 2020 | http://arc.aiaa.org | DOI: 10.2514/6.2000-1946

9. Rizk, Y. and Gee, K., "Numerical Prediction of the Unsteady Flowfield Around the F-18 at Large Incidence," AIAA Paper 91-0020, 29th Aerospace Sciences Meeting, Reno, NV, Jan. 1991.

10. Gee, K., Rizk, Y., and Schiff, L., "Effect of Forebody Tangential Slot Blowing on Flow About a Full Aircraft Geometry," AIAA Paper 93-2962, AIAA 24th Fluid Dynamics Conference, Orlando, FL, July 1993.

11. Gee, K., Murman, S., and Schiff, L., "Computation of F/A-18 Tail Buffet," Journal of Aircraft, Volume 33, Number 6, November-December 1996.

12. Rizk, Y., Guruswamy, G.P., and Gee, K., "Numerical Investigation of Tail Buffet on F-18 Aircraft," AIAA Paper 92-2673, AIAA 10th Applied Aerodynamics Conference, Palo Alto, CA, June 1992.

13. Ghaffari, F., Luckring, J.M., and Thomas, J.L., "An Overview of the Navier-Stokes Computations About the F/A-18 Aircraft with Multiblock Structured Grids," High Angle of Attack Technology Conference, Hampton, VA, September 1996.

14. "MATLAB User's Guide," The MathWorks, Inc., Natick, MA, August 1992.

15. Meyn, L.A., James, K.D., and Geenen, R.J., "Correlation of F/A-18 Tail Buffet Results," High-Alpha Projects & Technology Conference, NASA Dryden Flight Research Center, July 1994.

16. Moses, R.W. and Holt, A, "Spatial Characteristics of the Unsteady Differential Pressures on 16% F/A-18 Vertical Tails," AIAA-98-0519, 36th Aerospace Sciences Meeting and Exhibit, Reno, NV, January 1998.